Computational parametric study of a Richtmyer-Meshkov instability for an inclined interface

Jacob A. McFarland, Jeffrey A. Greenough, and Devesh Ranjan

Phys. Rev. E **84**, 026303 — Published 5 August 2011

DOI: 10.1103/PhysRevE.84.026303

Computational parametric study of a Richtmyer-Meshkov instability for an inclined interface

Authors

Jacob A. McFarland

Texas A&M University, Department of Mechanical Engineering, 3123 TAMU College Station, TX 77843

Jeffrey A. Greenough

Lawrence Livermore National Laboratory, 7000 East Ave. PO Box 808, L-95 Livermore, CA 94550

Devesh Ranjan*

Texas A&M University, Department of Mechanical Engineering, 3123 TAMU College Station, TX 77843

979-845-3580 (Tel)

979-845-3081 (Fax)

* Corresponding Author: dranjan@tamu.edu

Receipt Date

Original : February 08, 2011 Revised: May 4, 2011

Abstract

A computational study of the Richtmyer-Meshkov instability for an inclined interface is presented. The study covers experiments to be performed in the Texas A&M University inclined shock tube facility. Incident shock wave Mach numbers from 1.2 to 2.5, inclination angles from 30 to 60 degrees, and gas pair Atwood numbers of ~0.67 and ~0.95 are used in this parametric study containing 15 unique combinations of these parameters. Qualitative results are examined through a time series of density plots for multiple combinations of the parameters listed above, and the qualitative effects of each of the parameters are discussed. Pressure, density, and vorticity fields are presented in animations available online to supplement the discussion of the qualitative results. These density plots show the evolution of two main regions in the flow field: a mixing region containing driver and test gas that is dominated by large vortical structures, and a more homogenous region of unmixed fluid which can separate away from the mixing region in some cases. The interface mixing width is determined for various combinations of the above parameters. A new scaling method for the mixing width is proposed using the interface geometry and wave velocities calculated using one-dimensional gas dynamic equations. This model uses the transmitted wave velocity for the characteristic velocity and an initial offset time based on the travel time of strong reflected waves. The new model is compared to an adapted Richtmyer impulsive model scaling and shown to scale the initial mixing width growth rate more effectively for fixed Atwood number.

I. INTRODUCTION

The Richtmyer-Meshkov (RM) instability [1,2] is a hydrodynamic instability that develops due to misalignment of the pressure and the density gradients. This misalignment generates vorticity through the baroclinic term in the vorticity equation shown below in equation 1, where $\vec{\omega}$ is the vorticity, $D\vec{\omega}/Dt$ is the substantial derivative of $\vec{\omega}$, u is the velocity, v is the kinematic viscosity, ρ is the density, and p is the pressure.

$$\frac{D\vec{\omega}}{Dt} = \vec{\omega}\cdot\vec{\nabla}\vec{u} + v\nabla^2\vec{\omega} + \underbrace{\left[\frac{1}{\rho^2}\vec{\nabla}\rho\times\vec{\nabla}p\right]}_{Baroclinic\ term} \tag{1}$$

In the case of the RM instability the pressure gradient is created by an impulsive acceleration of a perturbed fluid interface. The vorticity deposited by this impulsive acceleration will cause the fluid interface to stretch and result in the mixing of the two fluids. The amount of the vorticity deposited will depend on the strength of the pressure and the density gradients. The Atwood number, as defined in equation 2 below, is a ratio of densities (ρ_h the higher density fluid and ρ_l the lower density fluid) at a fluid interface which can be used to describe the effects of the density gradient.

$$A = \frac{\rho_h - \rho_l}{\rho_h + \rho_l} \quad \text{(For the light-heavy case)} \tag{2}$$

The RM instability is an important phenomenon for inertial confinement fusion where its occurrence causes the fuel target to mix with inert material and reduces the fuel compression achieved. This reduction in compression greatly reduces the fusion yield. The RM instability is also important in stellar supernova where shock wave interaction with density discontinuities is an important feature. Accurate modeling of the RM instability is also important in the area of supersonic combustion, where understanding the mixing of fuel with air is crucial to improving performance. A summary of the RM instability and its applications is presented in the review article by Brouillette [3]. Another review of the RM instability focusing on the coherent structures formed in flowfield is presented by Zabusky [4].

Various methods for creating the RM instability for experiments have been developed and employed. A brief description of these methods is necessary for perspective on the method discussed in this paper. One method to generate the impulsive acceleration is to use a shock wave. Facilities using this method employ a mechanical shock tube to generate a shock wave which interacts with a fluid interface containing a density perturbation. An oscillation in the fluid interface can create a sinusoidal perturbation as implemented by Krivets *et al.* [5], and Motl *et al.* [6]. Another interface perturbation method employed in shock tubes is to use a bubble to contain a lighter or heavier gas as used by Ranjan *et al.* [7-9]. A third method is to employ a shaped falling gas curtain as described by Prestridge *et al.* [10]. A fourth method is to control the shape of the interface using a thin membrane as employed by Meshkov [2] in his seminal work, and by Brouillette and Sturtevant [11]. The effect of this membrane on the devolvement of the interface is examined by Houas and Chemouni [12], Abakumov *et al.* [13], and Erez *et al.* [14]. Finally, alternative methods to generate the impulsive acceleration have been developed as well. One of these methods is to use a sled device which has an impulsive acceleration created by dropping the test section onto a spring at the base of the sled track as described by Chapman and Jacobs [15].

For the study described in this paper the RM instability will be generated by passing a shock wave through a fluid interface. A simple perturbation in the fluid interface can be created by aligning the shock wave at an angle with respect to the density gradient, supported by gravity. This results in an inclined fluid interface with respect to the direction of the

impulsive acceleration. This is the method that will be employed in the Texas A&M University (TAMU) shock tube facility (Figure 1), currently under construction, to study the RM instability.

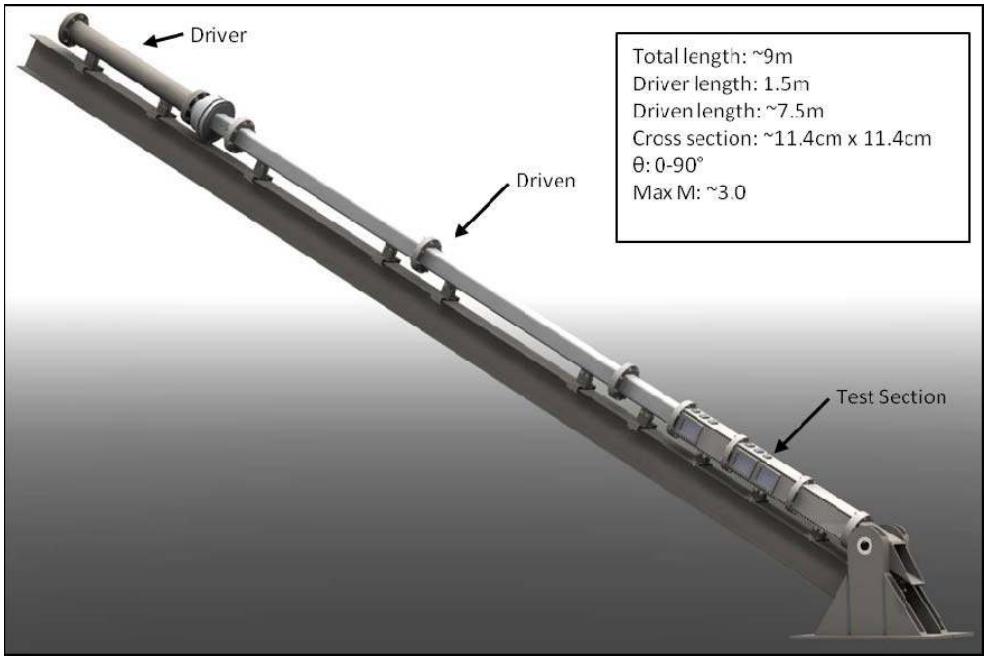

FIG. 1: Texas A&M University shock tube facility currently under construction

The simulations presented in the paper were performed in support of the TAMU shock tube facility design, and so the parameter space was limited to the capabilities of this facility. The TAMU shock tube facility will be capable of providing incident shock wave Mach numbers up to 3.0 in atmospheric pressure air, and will be capable of inclination from 0 to 90 degrees. The overall length of the shock tube will be approximately 9m. The test section is constructed with a modular design to allow for the interface to be imaged at wide range of times with interface visibility up to 1.5m downstream of its preshock position. Simultaneous measurements of density and velocity fields will be made using planar laser induced fluorescence (PLIF) and particle image velocimetry (PIV) systems.

II. COMPUTATIONAL SETUP

The computation study was performed using a staggered mesh Arbitrary Lagrange Eulerian (ALE) hydrodynamics code developed at Lawrence Livermore National Laboratory. The Lagrange time advancement is second-order predictor-corrector and uses the Gauss Divergence theorem to give the discrete finite difference equations [16]. All numerical differences are fully second order in space. Velocities are defined at mesh nodes and density and internal energy are defined at the zone centers using piecewise constant profiles. Artificial viscosity is used to suppress spurious oscillations [17]. A second-order remap [18] is applied to the solution after the Lagrange step. In all the simulations reported, a fixed Eulerian mesh is used at all times.

Boundary layers are included in these simulations by including a simple functional form for the viscosity, given in the next paragraph. The boundary conditions in these simulations are imposed as solid, no-slip, insulated walls. The no-slip wall boundary condition does generate a boundary layer, but is admittedly far from being resolved. Accurate resolution, however, is irrelevant to the current study. The ARES code includes an adaptive

mesh refinement (AMR) capability that allows the base resolution to be increased by a factor of three for each level of refinement. The refinement is performed on areas that exceed an error tolerance in the computation of a second undivided difference of density. The AMR approach implemented in ARES follows that of Berger and Oliger [19] and Berger and Colella [20]. Time advancement is not recursive though and the coarser levels are slaved to run at the finest level time step. This approach has been extensively studied and provides approximately a factor of 5-7 efficiency over a fully refined everywhere simulation.

A 2-D model was used for all simulations presented here. Viscosity was included using a model based on the Sutherland relation shown in equation 3 below, where μ is the dynamic viscosity, T is the temperature, and F_1 and F_2 are density and pressure correction factors. For these simulations both F_1 and F_2 were set to one. The various coefficients of the Sutherland relation for the gases used are presented in table I below. The inclusion of viscosity is briefly discussed in the appendix. The simulations presented in this paper did not include species diffusion, or stratification which will be included in future work.

(3) $$\mu = \left[\left(\nu_c + \nu_a \cdot \frac{T^{\nu_n}}{\nu_b + T} \right) F_1 \right] F_2$$

Table I: Summary of coefficients used in Sutherland relation.

Gas	ν_a (g/(cm μs $K^{1/2}$))	ν_b (K)	ν_c (g/(cm μs))	ν_n
Air	1.45E-11	110.4	0	1.5
SF_6	1.59E-11	243.8	0	1.5

Preliminary simulations were carried out with a computational domain that replicated the entire shock tube length and used to assess the associated x-t diagrams for the overall shock tube. To reduce computational times for the large number of runs required for this parametric study, the domain length was decreased to 2.5m. The shock wave was initialized 1cm ahead of the upstream most end of the interface, which varied in position for different inclination angles. The downstream and sidewall boundary conditions were reflecting walls with no slip conditions. The downstream wall was placed at similar position to that of a configuration of the TAMU shock tube to allow for more accurate simulations of reshock. A section of the computational domain for the initial conditions is shown below in figure 2 where the upstream and downstream boundary conditions are at x = 0 and x = 250 cm, respectively.

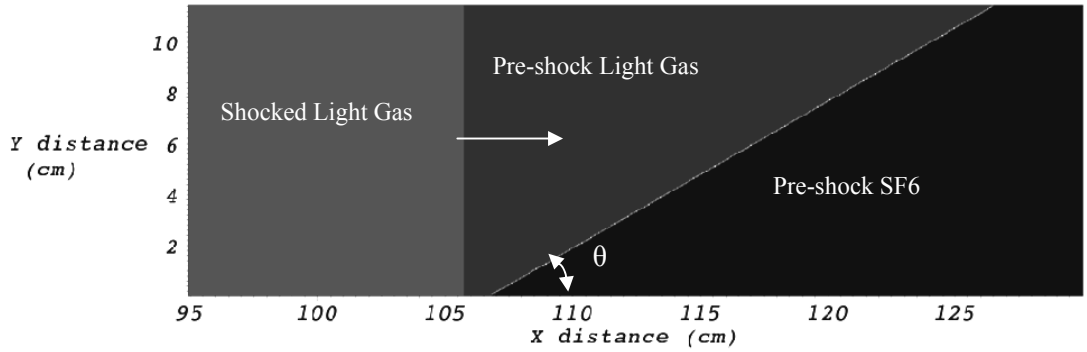

FIG. 2: Density plot of the initial conditions for an interface inclination angle of 30 degrees.

The upstream boundary consisted of a reflecting wall with a source term added to it which supplied the necessary mass inflow to support the shock wave. This boundary condition was not ideal, as the interface reflected shock waves traveling upstream were

reflected back towards the interface as expansion waves. The intersection of the reflected expansion waves with the shocked interface limited the time over which the simulation could be used to model experiments in the TAMU shock tube facility.

The parametric study was run for 3 different inclination angles; 30, 45, and 60 degrees. Two different gas pairs were used at each angle, air-SF_6 (A~0.67), and helium-SF_6 (A~.95). The air-SF_6 interface was run at three different Mach numbers: 1.5, 2.0, and 2.5. The helium-SF_6 interface was run at Mach 1.2 and 1.5. The resulting 15 cases are summarized below in Table II. AMR was invaluable for this study as it allowed for a rapid turn-around time for each run while efficiently allowing a higher resolution.

Table II: List of study simulations

Case	M	θ	Gas Pair
1	1.5	30	Air-SF_6
2	1.5	45	Air-SF_6
3	1.5	60	Air-SF_6
4	2.0	30	Air-SF_6
5	2.0	45	Air-SF_6
6	2.0	60	Air-SF_6
7	2.5	30	Air-SF_6
8	2.5	45	Air-SF_6
9	2.5	60	Air-SF_6
10	1.2	30	He-SF_6
11	1.2	45	He-SF_6
12	1.2	60	He-SF_6
13	1.5	30	He-SF_6
14	1.5	45	He-SF_6
15	1.5	60	He-SF_6

III. QUALITATIVE FLOW FIELD DESCRIPTION

A time series of density plots, for four different parameter sets, showing the effect of varying each of the 3 parameters is presented below in Figure 3. The exemplar (case 1, Fig. 3 set B, M_i=1.5, θ=30°, A~0.67) is displayed along with three other cases differing in incident shock Mach number (case 7, Fig. 3 set A, M_i=2.5, θ=30°, A~0.67), Atwood number (case 13, Fig. 3 set C, M_i=1.5, θ=30°, A~0.95), and interface inclination angle (case 3, Fig. 3 set D, M_i=1.5, θ=60°, A~0.67) respectively. Qualitatively, the flows all develop through the following stages:

- The incident shock wave encounters the inclined interface and generates a reflected shock wave and a transmitted shock wave.
- The reflected (transmitted) shock wave reflects off of the upper (lower) shocktube wall, interacting with the interface a second time.
- A region of SF_6 with low mixing evolves behind the transmitted shock front.
- This region can become disconnected (frame A4 of figure 3) from the mixing SF_6 fluid region or remain connected as in Frame D3 of figure 3.
- The transmitted shock wave re-planarizes and the low mixing region of SF_6 becomes rectangular in shape. This is most clearly seen in frame A4 of figure 3. In the remainder of the paper, we refer to this region of post shock SF_6 as the slug due to its rectangular shape.

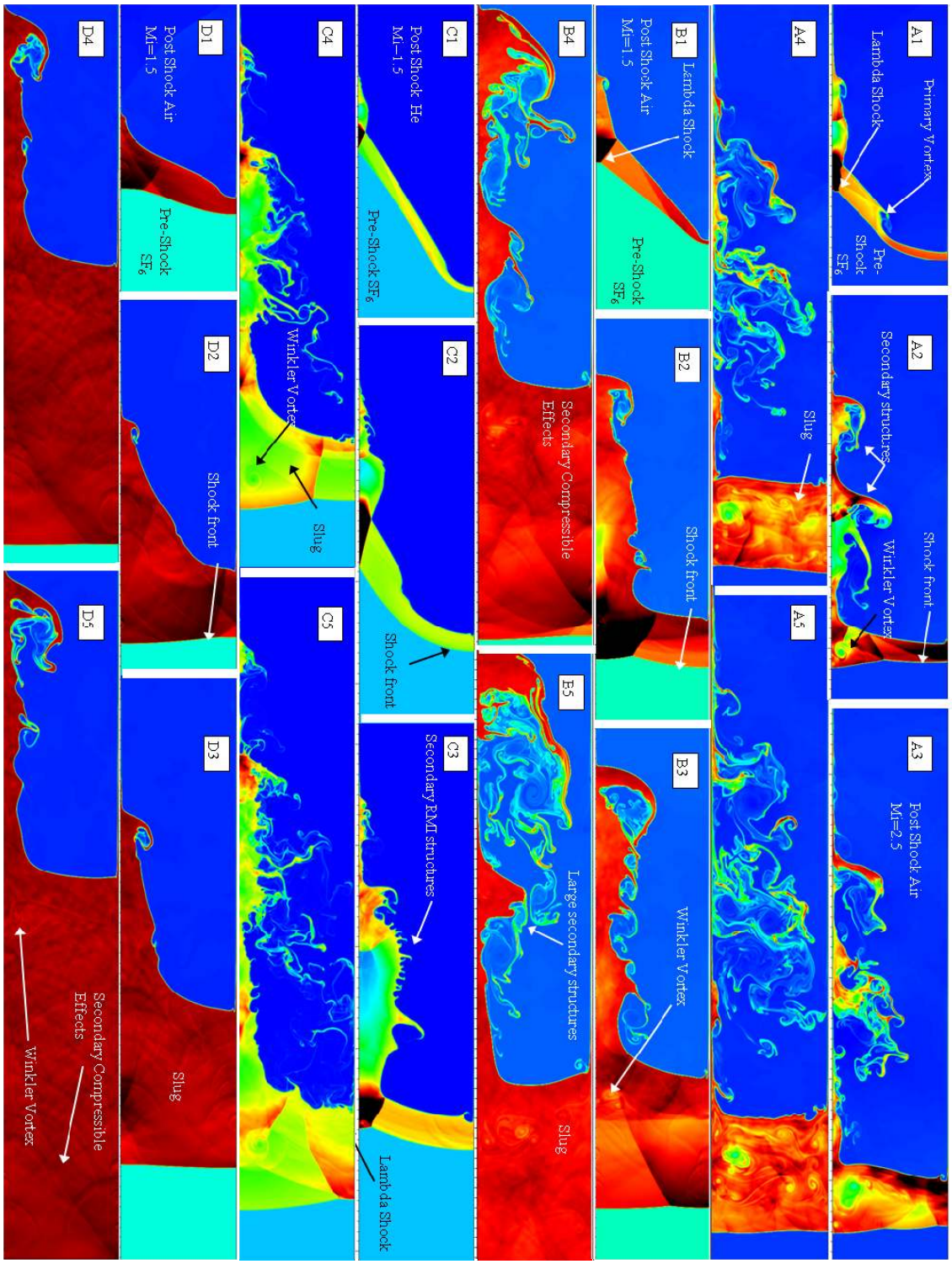

FIG. 3: (Color) Time series plot of density for three different parameter sets. Figures A1-A5, Case 7, at times 0.5, 1.0, 1.5, 2.0, and 2.5 ms respectively. Figures B1-B5, Case 1, at times 0.5, 1.5, 2.5, 4.0, and 5.5 ms. Figures C1-C5, Case 13, at times 0.25, 0.5, 1.0, 1.5, and 2.0 ms. Figures D1-D5, Case 3, at times 0.5, 1.5, 2.5, 4.0, and 5.5 ms.

Case 1 (Fig. 3, set B) will be used as the basis for comparison to the other three cases displayed in Fig. 3. This case is characterized by a large mixing region and slug. In this

scenario, a strong lambda shock wave (Fig.3, B1) is formed which travels up the slug until impacting and reflecting off the upper wall. This reflection creates many more secondary compressible effects of moderate strength that resonate within the slug (Fig. 3, B4). A weak Winkler type vortex structure [21] is formed within the slug (Fig. 3, B3). As the mixing region continues to develop in time, it separates into two large secondary vortical structures of SF_6, (Fig. 3, B5) which persist in the flow field to late times.

The effects of incident shock wave Mach number can be examined by comparing the case 1 (Fig.3, set B) with case 7 (Fig. 3, set A). In case 7, the stronger incident shock leads to a higher degree of separation between the mixing region and the slug. In this case the portion of the interface connecting the mixing region to the slug is flattened by a stronger interface reflected, upper wall reflected shock wave (illustrated in Figs. 8-10). The mixing region is separated by the primary vortex created at the upper wall (Fig. 3, A1) which has traveled down the interface. See supplemental material at http://link.aps.org/supplemental/DOI for an animation illustrating this process [22]. This separation results in the early destruction of the lambda shock allowing the primary transmitted shock to replanarize quickly. The destruction of the lambda shock and the limited width of the slug region suppress the secondary compressible effects within the slug that are seen in case 1. A strong Winkler type vortex structure is also created within the slug after the lambda shock is destroyed (Fig. 3, A2). The Winkler type vortex is joined by other smaller vortical structures at later times (Fig. 3, A5)

The effect of the interface Atwood number is shown by comparing case 1 (Fig. 3, set B) with case 13 (Fig. 3, Set C). It is worth noting that in case 13, the incident shock strength of Mach 1.5 in helium is more similar to the shock strength of case 7 (Mach 2.5) in air, and so it will be compared with this case as well. In case 13, the higher sound speed in helium increases the speed of shock waves reflected from the interface. The change in arrival times of reflected shocks ultimately results in the suppression of the large secondary structures seen in case 7 (Fig. 3, A2). In case 13 smaller secondary structures are created by a second refraction of the lambda shock with the interface. The strength of the refracted shock is weaker than that of case 1 and case 7, but its interaction with a relatively flat helium-SF_6 interface makes the secondary structures more visible.

Interface inclination effects can be highlighted by comparing the case 1 (Fig. 3, set B) with case 3 (Fig. 3, set D). Case 3 is characterized by slower interface growth and a smaller, less mixed, wall-bounded mixing region. The lower inclination angle (less oblique) provides particularly uniform properties in the post shock SF_6, due to the weaker reflected compressible effects (Fig. 3, D5). The weakness of reflected compressible effects also results in a simpler interface with fewer secondary spikes and limited mixing. However, a weak Winkler type vortex can be seen within the slug (Fig 3, D5) even in this case.

IV. QUANTITATIVE RESULTS

A. Early time growth rate scaling

Previous work on the scaling of growth rates was based on using linear growth models that are valid only in the linear growth regime. The linear growth regime is traditionally defined to be the period for which $\eta/\lambda<<1$, where η and λ are the interface mixing width (amplitude), and wavelength respectively [3,6]. For the interface discussed here, η/λ, as defined in section C below, is often near one before growth begins. However, the scaling provided by these linear growth models, with some adaptation as discussed in section C below, will be used to provide a first estimate of the scaling to be used for this new type of interface. Richtmyer [1] first proposed an impulsive growth model for a sinusoidal interface during the linear regime in 1960 based on Taylor's work on the Rayleigh-Taylor

instability of 1950 [23]. The impulsive growth model, is shown in equation 4, where [v], A', and η_0' are the interface velocity jump, post shock Atwood number, and post shock initial amplitude respectively.

(4) $$\dot{\eta}_0 = k[v]A'\eta_0'$$

To estimate the post shock amplitude, Meshkov [2] introduced the relationship given in equation 5 where w_i is the incident shock speed and η_0 is the pre-shock initial amplitude.

(5) $$\eta_0' = \eta_0\left(1 - \frac{|[v]|}{w_i}\right)$$

Various modifications to improve the impulsive model for both light/heavy and heavy/light interfaces have been made by Meyer and Blewett [24], and Vandenboomgaerde *et al.* [25]. A growth reduction factor was proposed for a diffuse interface by Motl *et al.* [6] based on the work by Brouillette and Sturtevant [11]. Compressible effects have been incorporated into linear growth models proposed by Fraley [26], Wouchuck and Nishihara [27], and Wouchuk [28].

While many attempts have been made to model the linear mixing width growth for sinusoidal interfaces, few have been presented for an inclined interface. It is worth noting that there is extensive literature on the shock refraction problem, where an inclined interface separating two gases is accelerated by a shock wave [29-32]. However, the post-shock acceleration flow was not well studied. Work on the post-shock flow has been limited thus far to numerical simulations and a few early experiments by Haas [33] and Sturtevant [34].Vorticity deposition on an inclined gas curtain was examined in simulations performed by Samtaney and Zabusky [35]. Numerical simulations to study vortex dynamics associated with an inclined gas curtain were presented by Zhang *et al.* [36]. The linear growth of arbitrary interface shapes, including a "v" shaped interface equivalent to an inclined interface, is studied in numerical simulations by Mikaelian [37].

B. Mixing width definition

Before a mixing width growth rate model can be applied and tested the mixing width must be defined. One method for defining the mixing width is to use the width for an equivalent perfectly mixed region. This is the procedure described by Cabot and Cook [38]. Another technique reported in literature define the mixing width as the distance between the 5 and 95% contour of the mole or mass fraction of one of the species. This method has the advantage of providing a length that has a physical representation in the experiments and is the one frequently used by experimentalists. It is however sensitive to "noise" , as isolated pockets of fluid can appear that intermittently perturb the mixing width (Fig. 4). The equivalent integral method is not subject to this effect. Nevertheless, we adopt the 5-95% method of computing the mixing width in the remainder of this paper, so that it can be compared easily to the future experimental results.

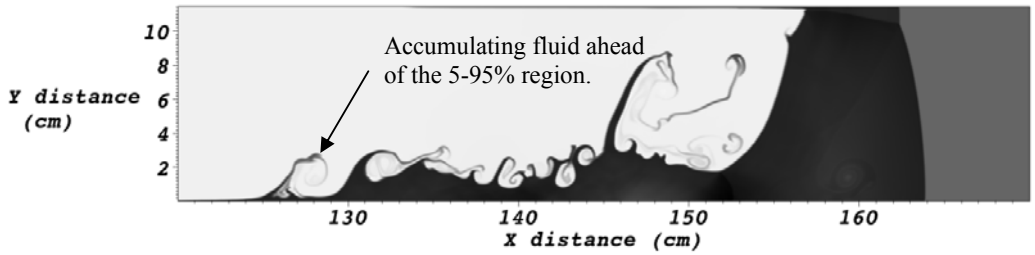

FIG 4: Density plot for case 14 showing accumulation of fluid outside of the calculated mixing width region (5%-95% species concentration).

C. Adaptation of Richtmyer impulsive model scaling

The adapted Richtmyer impulsive model (ARIM) scaling was tested as a first estimate to determine its ability to scale the simulation data and to guide the development of a new scaling method appropriate for the inclined interface. In adapting Richtmyer's impulsive model, we first define the amplitude and wavelength as shown in figure 5. The initial interface amplitude was defined as the length of the interface measured in the direction of travel of the incident shock wave (Figure 5). The interface wavelength was defined as twice the length of the interface perpendicular to the direction of travel of the incident shock wave. This is done since we view the interface as symmetric about the lower wall giving a triangular shaped initial condition which somewhat resembles the continuous sine wave for which Richtmyer's model was intended for.

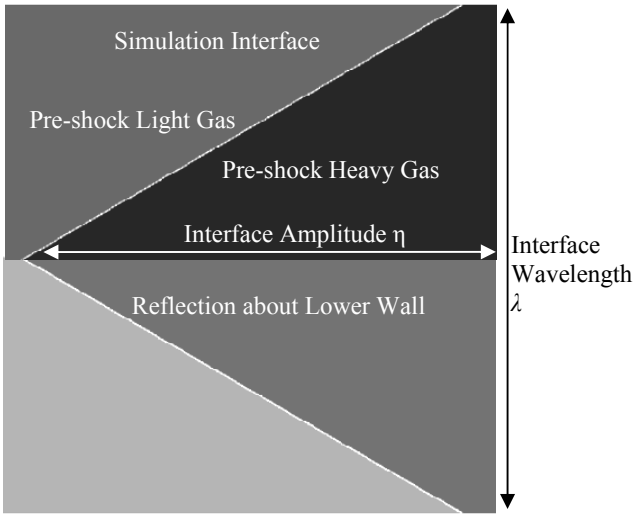

FIG. 5: Interface amplitude and wavelength for the adapted Richtmyer impulsive model scaling

Equations 6-10 define the ARIM used to analyze the simulations. Equation 6 defines a non-dimensional time, τ, with an offset time, t^*, that is the time required for the shock wave to traverse the inclined interface amplitude η, and is given explicitly in equation 9. This offset time is similar to the cloud-crushing time term, used in shock-bubble interactions literature **[7]**. A non-dimensional amplitude, $\overline{\eta}$, is also offset by the post-shock amplitude, η_0'. Equation 8 gives the impulsive growth rate from Richtmyer's model, and is similar to

equation 4, except here, we use the post-shock amplitude, η_0', at time t^* , as described in equation 10. Equation 10 ensures that the initial ARIM amplitude is zero, at $t = t^*$. The 1D gas dynamic parameters and wave speeds used in these calculations are given in Table III and IV below.

(6) $\tau = k\dot{\eta}_0 \left(t - t^*\right)$

(7) $\overline{\eta} = k(\eta - \eta_0')$

(8) $\dot{\eta}_0 = k\eta_0' A'[v]$

(9) $t^* = \lambda / \left(2w_i \tan\theta\right)$

(10) $\eta_0' = \eta\left(t^*\right)$

Table III: Gas dynamics properties.

Initial Parameters	Ratio of specific heats γ	Gas constant R (J/(kg K))	Initial Gas Temperature (K)	Initial Gas Pressure (kPa)
Air	1.4	287	300	101.3
Helium	1.667	2077	300	101.3
SF_6	1.09	56.92	300	101.3

Table IV: 1D gas dynamics calculated wave speeds.

Incident Mach Number	Light Gas	Heavy Gas	w_i (m/s)	w_t (m/s)	w_{rrt} (m/s)
1.2	Helium	SF_6	1223.00	192.73	156.34
1.5	Helium	SF_6	1528.76	282.05	177.56
1.5	Air	SF_6	520.75	242.76	156.56
2	Air	SF_6	694.38	353.75	167.23
2.5	Air	SF_6	867.97	465.55	197.17

The non-dimensionalized data from the ARIM scaling for the Air-SF_6 simulations is plotted below in Figure 6. For all mixing width plots, the key lists the cases described by the light gas name, the Mach number, excluding the decimal point, preceded by the letter M, and inclination angle preceded by the letter A. In Figure 6, the curves with constant angle of inclination and different incident shock strengths appear to collapse well. The scaling does not account for the angle of inclination in its current form.

For early times, say $\tau < 5$, the collapse is not as good as it is at later τ. This is partially due to the discontinuities in mixing width measurements discussed in section B above, but also due to the initial non-linear growth that occurs after the incident shock wave traverses the interface initial amplitude. The data is cropped at the onset of reshock from the downstream boundary. Sudden increases in the mixing width are visible towards the end of some data sets. These sudden increases are due to the mixing width definition errors discussed in section B.

Figure 7 below shows non-dimensionalized helium-SF_6 simulation data compared to a sample of the Air-SF_6 data for comparison. Overall it is seen that the collapse is poor, but that the helium-SF_6 simulations fall in the same range of non-dimensional growth rates as the air-SF_6 simulations. This is encouraging and suggests that the ARIM scaling is collapsing the data well for different Atwood numbers but not accounting for the different initial interface inclination angles correctly.

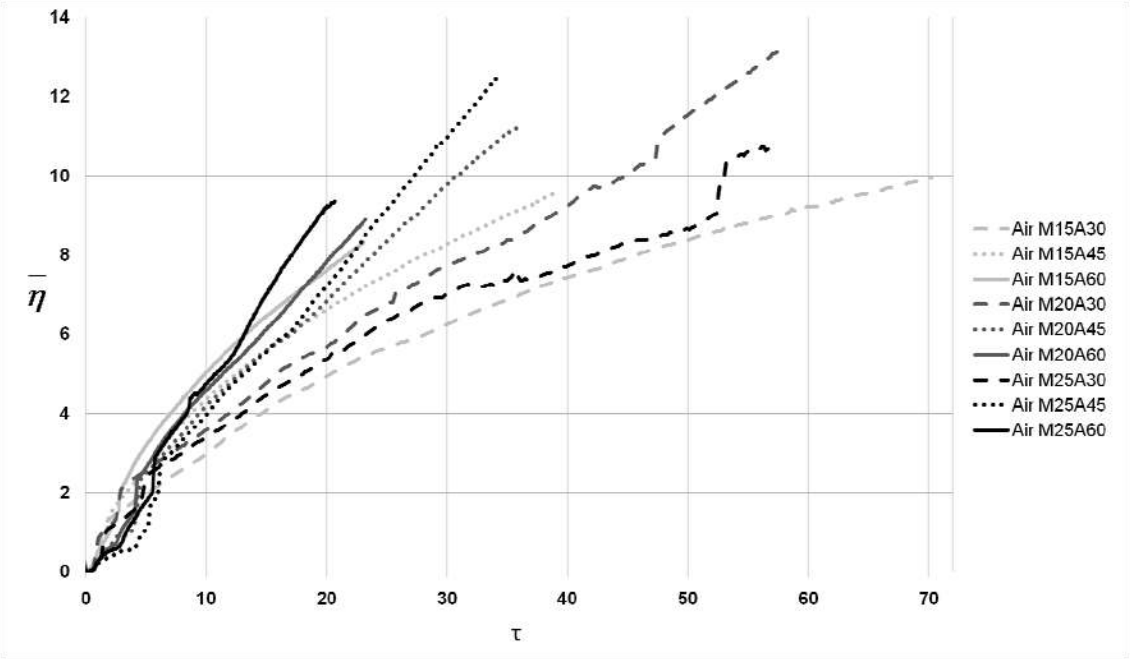

FIG. 6: Non-dimensional mixing width versus time for all air-SF_6 parameter sets where $\overline{\eta}$ is the non-dimensional mixing width, and τ is the non-dimension time.

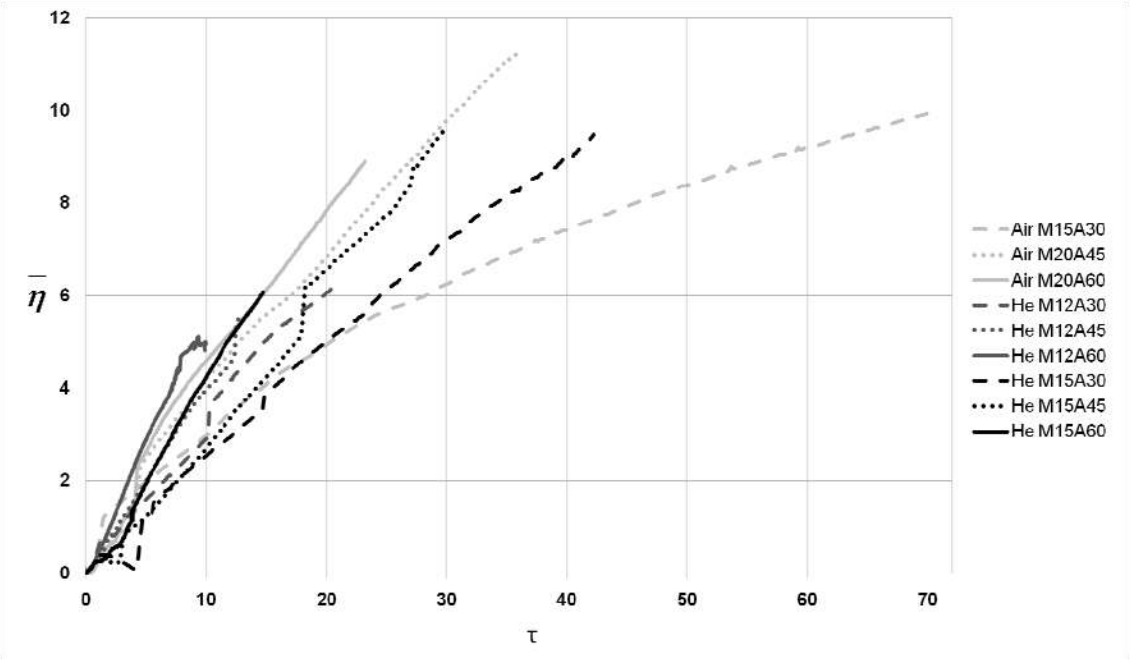

FIG. 7: Non-dimensional mixing width versus time for selected air-SF_6 and helium-SF_6 parameter sets where $\overline{\eta}$ is the non-dimensional mixing width, and τ is the non-dimension time .

D. Inclined interface scaling

It appears that the ARIM scaling must be adjusted to account for the interface geometry and the initial non-linear compression of the interface. The strategy for arriving at a new early time, inclined interface scaling(IIS) was to use the basic pattern of the Richtmyer impulsive model scaling but to select parameters appropriate to an inclined interface. The Richtmyer impulsive model scaling consists of an offset time multiplied by a gas pair ratio and divided by characteristic time (equation 11). Since the ARIM scaling matched different Atwood number cases well, the gas pair ratio parameter, Atwood number, was not changed.

$$\tau = \frac{A\left(t - t^{*}\right)}{t_{char}} \tag{11}$$

The characteristic time in the Richtmyer impulsive model scaling was found from a characteristic velocity, the interface jump velocity, and a characteristic length, the wave number squared divided by the post shock interface amplitude. For the IIS it was found that the transmitted shock wave speed (w_t) was a more accurate characteristic velocity. This is because the important secondary compressible effects (interface reflected, wall reflected, interface transmitted ($I_R W_R I_T$) shock wave, and subsequent reflections) travel at speeds that scale more closely with the transmitted wave speed. The importance of these secondary compressible effects is explained further with respect to the selection of an offset time later.

The characteristic length was selected by examining the effects of the length of the interface parallel (height) and perpendicular (width) to the incident shock wave velocity. The result was a characteristic length term called, the effective λ given by equation 12. This term can be described as the interface width that would be required for each inclination angle if the interface height were held constant across all inclination angles, θ (as defined in Fig. 2). The resulting characteristic length is defined as $\lambda^2 / \left(2\eta_0\right)$. This is similar to the characteristic length for the ARIM scaling ($\lambda^2 / 4\pi^2\eta_0'$). The difference between the two scaling methods is that the ARIM scaling uses the post shock compressed amplitude, whereas the IIS uses the initial interface height.

$$\lambda_E = \lambda \cdot \tan(\theta) \tag{12}$$

Another difference in the IIS method was to use a more accurate offset time to better predict the initial non-linear compression time. The ARIM scaling was offset by the time it took for the incident shock wave to traverse the height of the interface. This accounts for the initial compression of the interface by the incident shock wave but misses the compression effects of the secondary compressible waves. After the incident shock wave is transmitted, secondary compression and expansion waves continue to traverse the width of the interface. These waves increase in strength as the interface inclination angle becomes more oblique (smaller θ). The strength of these waves diminishes with every subsequent interaction with an interface or boundary that occurs.

The first of these secondary effects is shown below in Figure 8. This wave is denoted as the interface reflected, wall reflected ($I_R W_R$) shock wave. The strength of this shock wave is sufficient to cause a compression of the interface along its width, and to extend the initial non-linear compression time of the interface. Subsequent waves will continue to alter the growth rate at a diminishing rate. The time at which this wave has compressed the interface will approximate the end of the initial non-linear compression time.

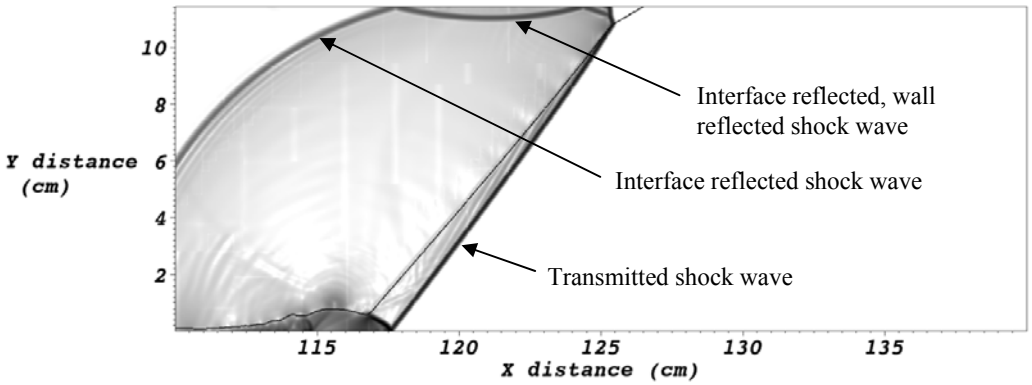

FIG. 8: Gradient of pressure field plot at early time (*t*~.226ms) for case 7.

To predict the time at which the I_RW_R shock wave has compressed the interface, 1D gas dynamic equations were used. The initial compression time from the incident shock wave was again calculated using the 1D incident shock speed and the interface height. At the end of this time it was assumed that part of I_RW_R shock transmits through the interface. The transmitted leg of this wave ($I_RW_RI_T$) was used to determine the end of the initial nonlinear compression time since it had the lower speed. While the 1D calculated speed of the un-transmitted leg of the wave is higher, the wave is limited by the transmitted leg (Figure 9). Using the 1D approximated speed of the transmitted leg more accurately predicted the time at which the transmitted leg has reached the wall (Figure 10) and the compression of the interface from this wave is complete. The width compression time is then determined from the 1D velocity of the $I_RW_RI_T$ shock wave (w_{rrt}), and the width of the interface. This time is added to the initial compression time to yield the new offset time shown in Equation 13.

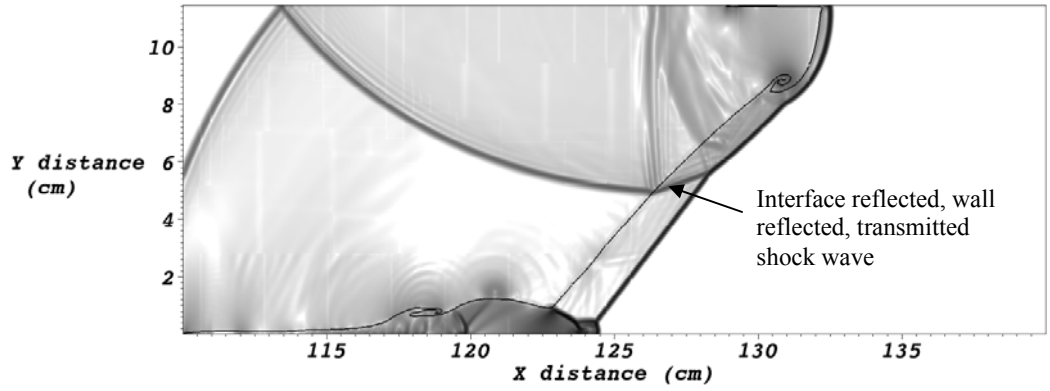

FIG. 9: Gradient of pressure field plot (*t*~.302ms) for case 7.

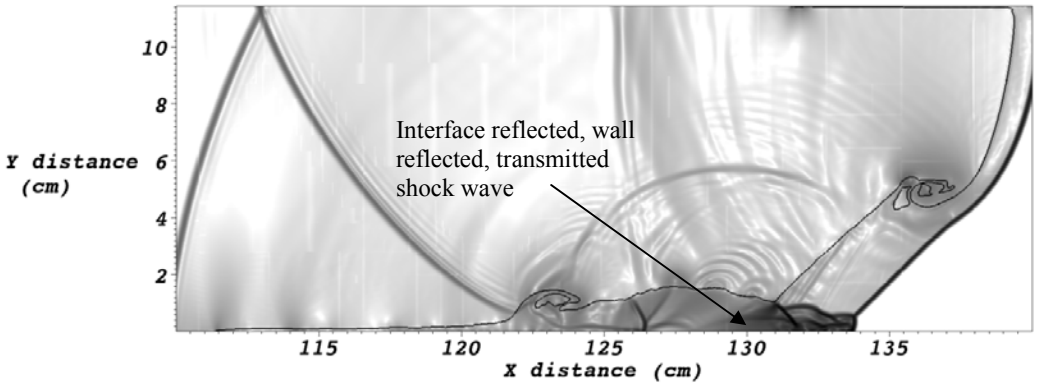

FIG. 10: Gradient of pressure field plot (*t*~.524ms) for case 7.

Equations for the IIS method are summarized in equations 13-16. The calculated 1D transmitted wave speeds used in equations 13 and 14 can be found in Table IV of the previous section. The results of the IIS are presented below in figures 11 and 12. It can be seen in figure 11, that there is less scatter in the data, as compared to figure 6. Furthermore the shape of the scaled curves is much more linear. The IIS method appears to account better for the nonlinearity of the problem as well as for the angle of inclination. However, it would appear from figure 12, that the agreement between helium-SF_6 cases is not as good. The errors associate with the mixing width algorithm, discussed in section B, creates artificial jumps in the mixing width data that then offset the non-dimensional mixing width. If the slopes after these jumps are compared to each other, it can be seen that the growth rates are similar for all cases. Also in Figure 11 (air-SF_6) these jumps in the mixing width can be seen to cause an artificial divergence in the data at very early times (near τ_a=0). A different definition of the mixing width or a modification of the current definition could mitigate these jumps, and will be considered in future work. However, it is worth noting, that this method of calculating mixing width is frequently used by the experimentalists and therefore provides a base for experimental verification of our scaling.

$$(13) \qquad t_a^* = \frac{\lambda}{2w_i \tan\theta} + \frac{\lambda}{2w_{rrt}}$$

$$(14) \qquad \tau_a = \frac{w_t A'}{\lambda_E}\left(t - t_a^*\right)$$

$$(15) \qquad \overline{\eta}_a = \frac{\left(\eta - \eta^*\right)}{\lambda_E}$$

$$(16) \qquad \eta^* = \eta(t_a^*)$$

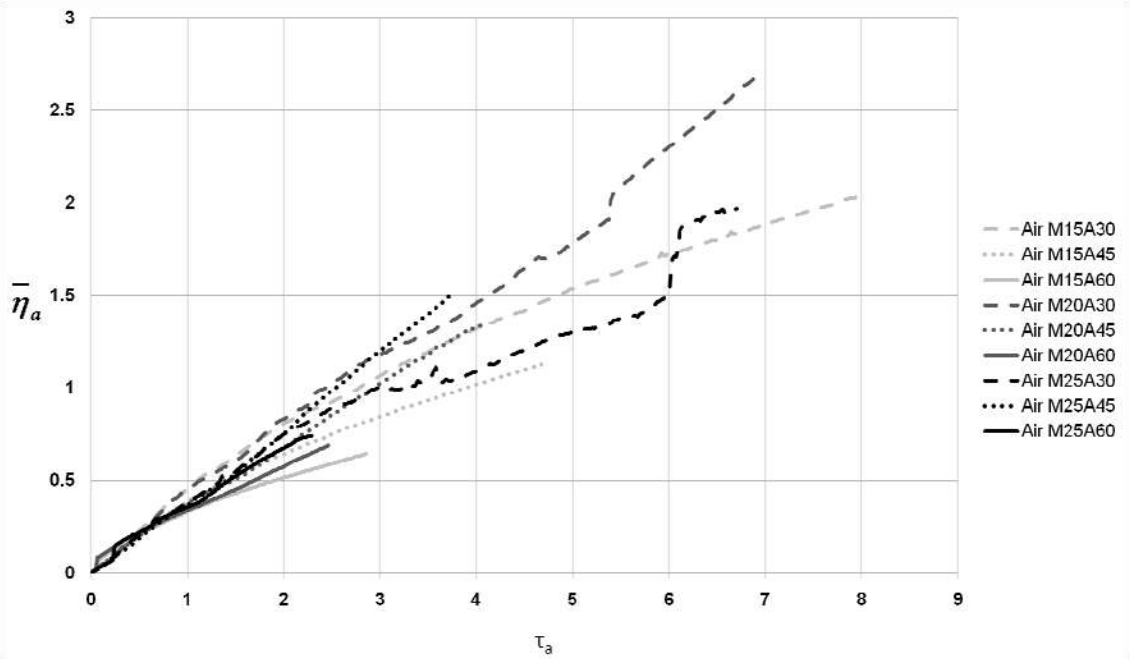

FIG. 11: Non-dimensional mixing width versus time for all air-SF_6 parameter sets where $\overline{\eta}_a$ is the non-dimensional mixing width, and τ is the non-dimension time defined using the new scaling method.

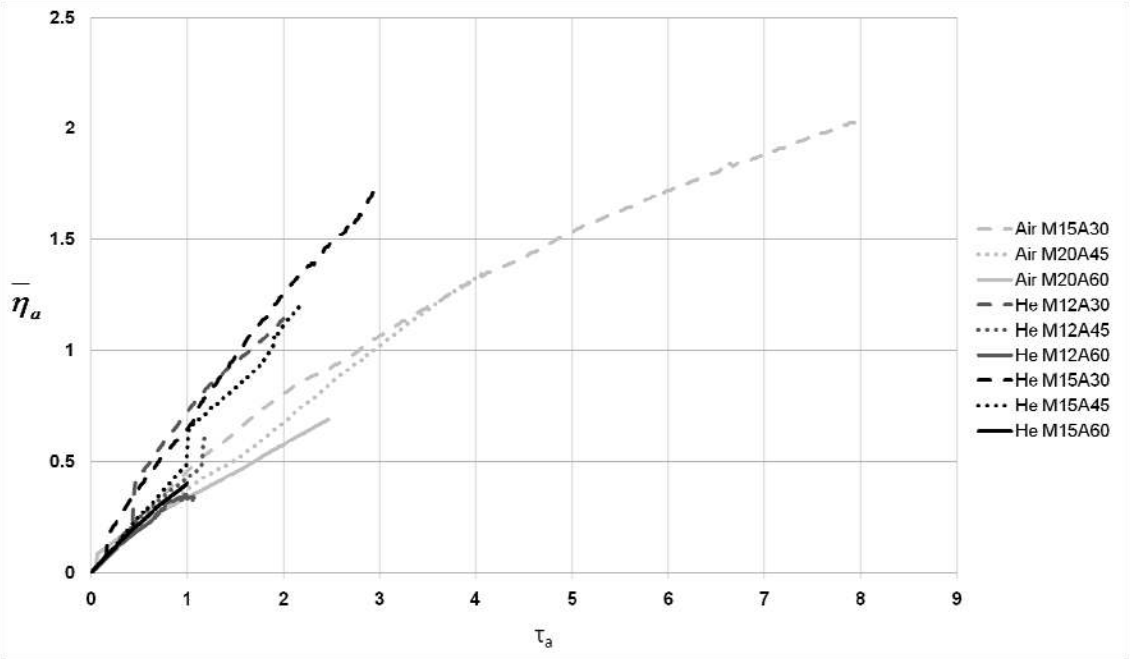

FIG. 12: Non-dimensional mixing width versus time for selected air-SF_6 and helium-SF_6 parameter sets.

To compare the performance of the two scaling methods the coefficient of variance (standard deviation / mean) was plotted for the air-SF6 cases in figure 13. The coefficient of variation shows how well data from different cases are collapsing to a single line (the mean),

where a lower value indicates the data is closer to a common line. Comparing the coefficient of variance for the two different scaling methods is complicated because the two scaling methods do not have a common τ, nor can the two non-dimensional times be scaled to each other. To attempt a fair comparison of the two scaling methods the non-dimensional mixing width was compared between two common events, the start of the shock-interaction with the interface (τ,τ_a=0) and the first reshock that occurs. This reshock occurs in the M=2.5, θ=60° case for both scaling methods. Figure 13 shows the coefficient of variance is lower for the IIS method. The IIS method shows a large improvement at early times with the exception of the spike at τ_a of approximately 0.1. This spike is an error again due to an artificial rise in the mixing width created by the mixing width definition discussed in section B. If the error which produced the spike was resolved the new scaling method should result in less than a 10% deviation from the mean non-dimensional mixing width up to τ_a of 0.85. The deviation only increases to approximately 15% at τ_a of 2 where the first reshock occurs. The helium-SF_6 data showed similar improvement when plotted alone as well as when incorporated with the air-SF6 data but neither scaling method performed well at higher Atwood numbers.

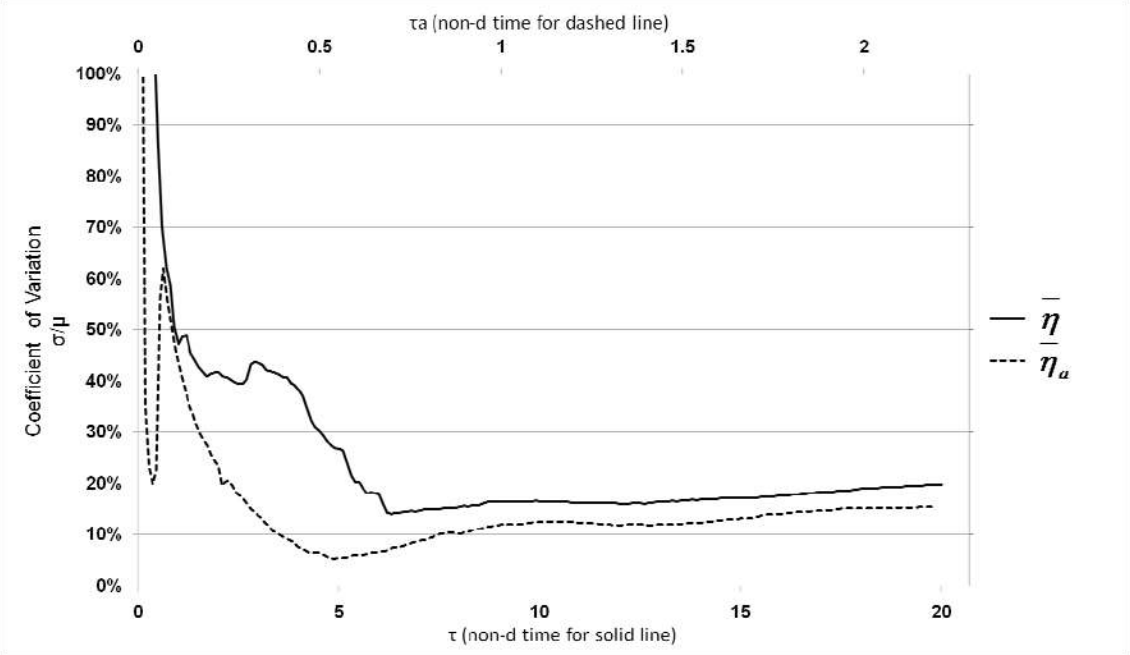

FIG. 13: Coefficient of variation for the non-dimensional mixing width plotted for air SF_6 where $\bar{\eta}$ is the non-dimensional mixing width for the adapted Richtmyer impulsive model scaling and $\bar{\eta}_a$ is the non-dimensional mixing width for the new scaling method.

V. CONCLUSIONS

From flow-field visualization of the inclined interface problem, within the parameter space studies here, it is seen that the post-shock flow field is sensitive to the details of the initial shock refraction problem. These density plots show the evolution of two main regions in the flow field: a mixing region containing driver and test gas that is dominated by large vortical structures, and a more homogenous region of unmixed fluid which can separate away from the mixing region in some cases. The early time growth rate of the mixing width is predicted poorly using the Richtmyer impulsive model scaling as adapted in this paper for the

inclined interface. The adapted Richtmyer impulsive model scaling struggles to collapse the data from different inclination angles. A new scaling method, the Inclined Interface Scaling (IIS) method, was proposed that collapses the data for different incident shock wave Mach numbers, and interface inclination angles well at early times by using more detailed information about the complex shock refraction problem. The IIS method improved agreement for different Atwood numbers but still requires some improvement. This method uses the 1D gas dynamics wave speeds for the incident shock wave and the interface reflected, wall reflected, and transmitted shock waves to predict the end of the initial nonlinear compression of the interface. The characteristic velocity for the IIS method was the 1D transmitted wave speed instead of the interface jump velocity used in the classical Richtmyer impulsive model. It is anticipated that the future experiments, coupled with ongoing simulation work, will be able to shed light on the secondary effects at late times and hence explore the divergence seen in the data.

ACKNOWLEDGEMENTS

The authors would like to thank the anonymous reviewers for their valuable comments and suggestions to improve the quality of the paper. Jacob A. McFarland would like to thank Robert Morgan, and Chris Weber for the consultation, advice and support while this research was conducted. Also, to thank Prof. Riccardo Bonazza for his advice and helpful discussion of the work presented in this paper. Additionally this work could not have been performed without the support of High Energy Density Physics Summer Student Program which provided Jacob A. McFarland with the opportunity to work with highly knowledgeable and helpful employees of LLNL. Finally, this work performed under the auspices of the U.S. Department of Energy by Lawrence Livermore National Laboratory under Contract DE-AC52-07NA27344.

APPENDIX A: RESOLUTION STUDY

A resolution study was first performed to determine the maximum resolution that could be achieved while limiting the simulation computer run times to a level that would allow the study to be completed in a two month period. The most computationally time intensive simulation used the following parameters; incident shock wave Mach number of 2.5, interface inclination angle of 30°, and an Atwood number of ~0.67 (air-SF_6 interface). Several simulations were started for this set of parameters with different resolutions to estimate the computation time it would take for the models to run to 4ms. This time was chosen as the cutoff point as it would run long enough for reshock to be captured, but would stop the simulation before expansion waves reflected from the upstream boundary could intersect the interface. The viscosity model was not included in these resolution study simulations because the viscosity study and consequent decision to include viscosity was dependent on the resolution study.

All but two of these simulations were stopped at less than 0.1 ms simulation time. Two simulations, at 282 μm and 56 μm resolutions, were run out to a time of 0.5ms where the interface had developed long enough for a qualitative comparison to be made. Density plots of these two simulations are shown below in Figure 14. It can be seen from these plots that the 56 μm resolution case showed fine structures that one would expect to be damped out by species diffusion. Since species diffusion could not be included in the simulations the 282 μm resolution simulation provides a more density plot that is expected to match experiments more closely. Computational times for these simulations were significantly different as well. These simulations were run on 128 cores total, where each node consisted of AMD Optetron quad core processors with 16 cores and 32GB of memory per node. The 56 μm resolution case required and estimated 130hrs to run, and the 282 μm case required 7hrs. The next incremental increase in resolution (169 μm) gave an estimated run time of 32 hrs. Based on the computational times the 282 μm resolution was selected for the parametric study.

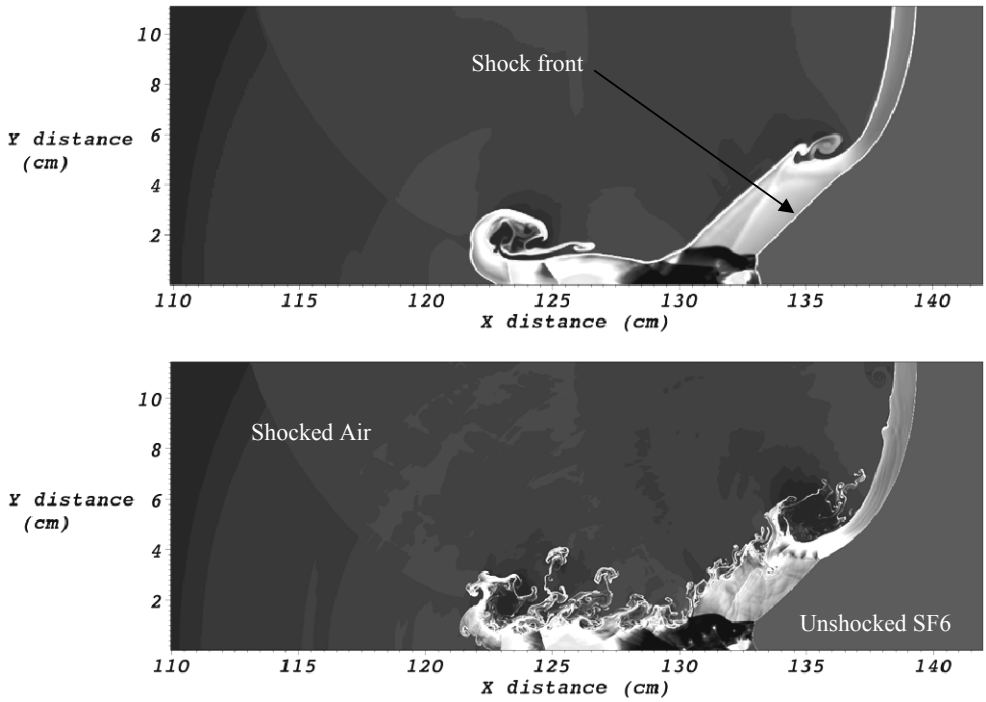

FIG. 14: Density plot for M=2.5, θ=30°, and A~0.67 (air-SF_6 gas pair) at t=0.5ms. Top: resolution of 282 µm. Bottom: resolution of 56 µm.

APPENDIX B: VISCOSITY STUDY

After selecting the resolution for the parametric study, a comparison was made between a viscous simulation and an inviscid simulation. The same parameters used in the resolution study were again applied, incident shock Mach number of 2.5, inclination angle of 30 degrees, and air-SF_6 gas pair. Each simulation was run to greater than 4ms to allow late time and reshock development to be compared. Figure 15 below shows density plots for the viscous and inviscid cases at approximately 1ms. From these plots it can be seen that the addition of viscosity has a significant damping effect on the growth of secondary spikes. The addition of viscosity has also slowed the transmitted wall reflected shock wave due to the presence of a boundary layer and stretched the interface due to the no slip condition at the wall. At later times the difference becomes more significant but more difficult to define. The viscous model was chosen because of the significant differences in the interface growth. Including viscosity in the simulation increased the computational time from 7 hours to 11 hours for the parameters M=2.5, θ=30°, air-SF_6.

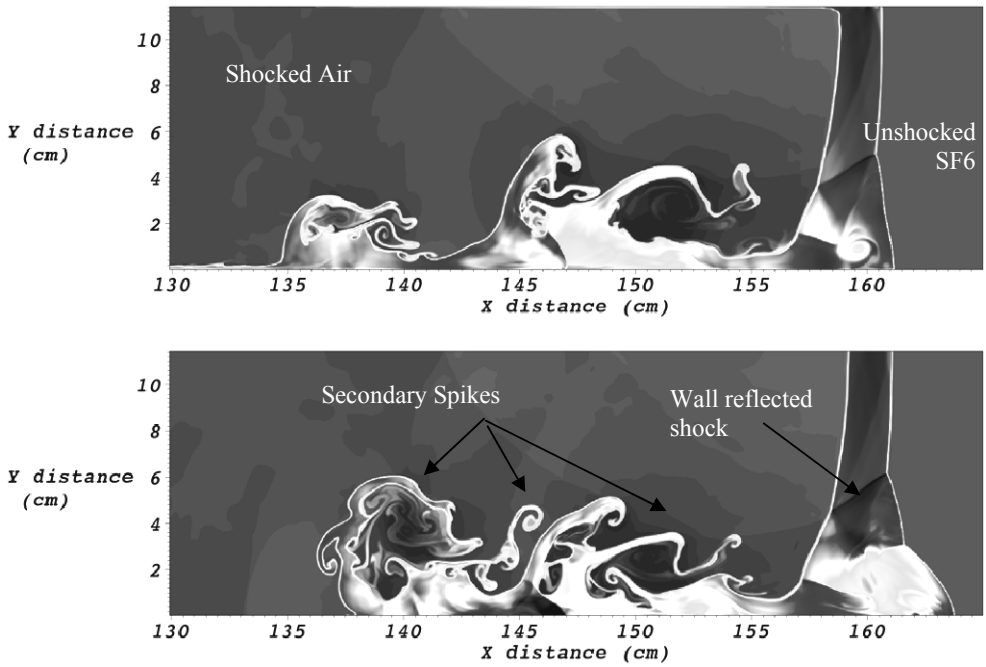

FIG. 15: Density plots for M=2.5, θ=30°, and A~0.67 (air-SF_6 gas pair) at t=1ms. Top: viscous model. Bottom: inviscid model.

REFERENCES

[1] R. D. Richtmyer, Comm. Pure Appl. Math. **13**, 297-319 (1960).
[2] E. E. Meshkov, Fluid Dyn **4**, 101-104 (1972).
[3] M. Brouillette, Annual Review of Fluid Mechanics **34**, 445–468 (2002).
[4] N. J. Zabusky, Annual Review of Fluid Mechanics **31**, 495–536 (1999).
[5] V. V. Krivets, C. C. Long, J. W. Jacobs, and J. A. Greenough, Shock Waves 1205–1210 (2009).
[6] B. Motl, J. Oakley, D. Ranjan, C. Weber, M. Anderson, and R. Bonazza, Physics of Fluids **21**, 126102 (2009).
[7] D. Ranjan, M. Anderson, J. Oakley, and R. Bonazza, Physical Review Letters **94**, 184507 (2005).
[8] D. Ranjan, J. Niederhaus, B. Motl, M. Anderson, J. Oakley, and R. Bonazza, Phys. Rev. Lett. **98**, (2007).
[9] D. Ranjan, J. Oakley, and R. Bonazza, Annual Review of Fluid Mechanics **43**, (2011).
[10] K. Prestridge, P. Vorobieff, P. M. Rightley, and R. F. Benjamin, Physical Review Letters **84**, 4353–4356 (2000).
[11] M. Brouillette and B. Sturtevant, Physics of Fluids A-Fluid Dynamics **5**, 916–930 (1993).
[12] L Houas and I Chemouni, Physics of Fluids **8**, 614 (1996).
[13] A. I. Abakumov, V. Y. Fadeev, S. I. Kholkin, E. E. Meshkov, V. V. Nikiforov, P. N. Nizovtzev, N. N. Sadilov, S. K. Sobolev, V. A. Tilkunov, V. O. Tochilin, and others, in *Proceedings of the Fifth International Workshop on Compressible Turbulent Mixing, Edited by R. Young, J. Glimm, and B. Boston (World Scientific, Singapore, 1996)* (n.d.), p. 118.
[14] L. Erez, O. Sadot, D. Oron, G. Erez, L. A. Levin, D. Shvarts, and G. Ben-Dor, Shock Waves **10**, 241–251 (2000).
[15] P. R. Chapman and J. W. Jacobs, Physics of Fluids **18**, 074101 (2006).
[16] M. L. Wilkins, *Calculation of Elastic Plastic Flow* (University of California Lawrence Radiation Labratory, 1963).
[17] T. V. Kolev and R. N. Rieben, Journal of Computational Physics **228**, 8336–8366 (2009).
[18] R. W. Sharp and R. T. Barton, *HEMP Advection Model* (Lawrence Livermore Labratory, 1981).
[19] M. J. Berger and J. Oliger, Journal of Computational Physics **53**, 484–512 (1984).
[20] M. J. Berger and P. Colella, Journal of Computational Physics **82**, 64–84 (1989).
[21] K. H. A. Winkler, J. W. Chalmers, S. W. Hodson, P. R. Woodward, and N. J. Zabusky, Physics Today 29 (1987).
[22] J. McFarland, EPAPS Documents (2011).
[23] G. Taylor, Proceedings of the Royal Society of London. Series A, Mathematical and Physical Sciences 192–196 (1950).
[24] K. A. Meyer and P. J. Blewett, Phys. Fluids **15**, 753 (1972).
[25] M. Vandenboomgaerde, C. M\ügler, and S. Gauthier, Physical Review E **58**, 1874–1882 (1998).
[26] G. Fraley, Physics of Fluids **29**, 376 (1985).
[27] J. G. Wouchuk and K. Nishihara, Physics of Plasmas **3**, 3761–3776 (1996).
[28] J. Wouchuk, Phys. Rev. E **63**, (2001).
[29] R. G. Jahn, Journal of Fluid Mechanics **1**, 457-489 (1956).
[30] A. M. Abd–El–Fattah, L. F. Henderson, and A. Lozzi, Journal of Fluid Mechanics **76**, 157–176 (1976).
[31] A. M. Abd-El-Fattah and L. F. Henderson, Journal of Fluid Mechanics **86**, 15–32 (2006).
[32] A. M. Abd-el-Fattah and L. F. Henderson, Journal of Fluid Mechanics **89**, 79–95 (1978).
[33] J. F. Haas, in *Proceedings of the 19th International Symposium on Shock Waves* (Springer, Marseille, France, 1993), pp. 27-36.
[34] B. Sturtevant, in *16th International Symposium on Shock Tubes and Waves* (Aachen, West Germany, 1987), pp. 89-100.
[35] R. Samtaney and N. J. Zabusky, Journal of Fluid Mechanics **269**, 45–78 (2006).
[36] S. Zhang, G. Peng, and N. J. Zabusky, J. of Turbulence **6**, (2005).
[37] K. O. Mikaelian, Phys. Fluids **17**, 034101 (2005).
[38] W. H. Cabot and A. W. Cook, Nat Phys **2**, 562-568 (2006).